Substructure Characterization of a 16-8-2 GTA Weld Through Transmission Electron Microscopy

Differences between weld and base metal that are presumably characteristic of all weld deposits provide, for the first time, a fundamental explanation of why welds behave differently than base metals

BY J. R. FOULDS AND J. MOTEFF

ABSTRACT. A weldment section from "formed and welded" 0.91 m (35.8 in.) OD diameter 12.77 mm (½ in.) thin wall Type 316 stainless steel pipe primarily for structural use in the hot-leg of the liquid-metal fast breeder reactor is characterized microstructurally through Transmission Electron Microscopy (TEM). The GTA weldment, welded with 16-8-2 filler metal, is sectioned from pipe in the "formed + welded + solution-annealed + straightened" as well as the "formed + welded + solution-annealed + straightened + re-solution-annealed" condition.

The optically seen weld metal dendritic substructure, when viewed through TEM, appears as a dislocation substructure with low-angle (<1.0 deg misorientation) boundaries demonstrated to be stable on reannealing and built up on interdendritic planes of mismatch. The substructure size and subboundary energy or misorientation are shown to be affected by variations in the weld heat-input rate.

Subboundary analyses indicate the "build-up" or "polygonization" occurs on immobile "growth" dislocations accommodating the mismatch between adjacently growing dendrites during weld pool solidification. Residual weld metal strengths, even after annealing, are attributed to these stable subboundaries through a decrease in the "effective" grain size. In fact, this study represents the first step in explaining weld/base metal mechanical behavior differences. These often subtle but consistent differences are explainable by consequences of the very nature of weld pool solidification, stable solidification dislocation substructures.

J. R. FOULDS is a Research Associate and J. MOTEFF a Professor, Department of Materials Science and Metallurgical Engineering, University of Cincinnati, Cincinnati, Ohio.

Introduction

Much of the research in the area of austenitic stainless steel welding has been understandably concerned with the establishing of a "macroscopic" compatibility between weld and base metal through variations in the welding process and parameters. "Macroscopic" here refers to the resulting chemistry, optically-observed grain structures, and results of conventional nondestructive inspection techniques as applied to weldments. This "macroscopic" weld/base metal compatibility, however, does not explain consistent differences between weld and base metal elevated temperature mechanical behavior.

The most recent high temperature mechanical property data (Ref. 1) on automatic gas tungsten-arc girth welded (with 16-8-2 filler metal) large diameter Type 316 stainless steel pipe weldments show a higher yield strength, lower ultimate tensile strength, lower stress-rupture life and stress-minimum creep rate curves for the weld metal as compared with the base metal. The observations, in fact, represent a general comparison of weld and base metal elevated temperature mechanical behavior seen for a variety of austenitic stainless steel weldments. In each case, profferred explanations for these based on chemistry and grain size have been unable to explain all the property differences; moreover, they have been found wanting with regard to possible generalizations to other weldments.

Beyond the "macroscopic" compatibility mentioned above, the subtle but consistent weld/base metal behavior differences must be explainable by consequences of the very nature of the weld poor solidification process. As a first step in understanding weld metal mechanical behavior based on its characteristic dendritic structure, a 16-8-2 GTA seam-welded Type 316 stainless steel pipe weldment section has been substructurally characterized using the Transmission Electron Microscope (TEM). The primary application of the material investigated here is that of a structural piping component in the hot-leg of the liquid-metal fast breeder reactor. Nonetheless, the results of this characterization may be applicable not only to all welds, but also to all rapidly-solidified crystallographic systems.

Experimental Procedure

Material

The 0.91 m (35.8 in.) OD diameter 12.77 mm (½ in.) thin wall Type 316 stainless steel pipe was manufactured in 1.83 m (6 ft) lengths by a commercial vendor through a forming and longitudinal seam-welding process as per ASME

Table 1—Fabrication Data on Formed and Welded Pipe Studied

ASME code, section II, material specification:	
Plate	SA-240 (Ref. 2)
Pipe	SA-358 (Ref. 3)
ASME code, section III:	
Class	1 (Ref. 4)
Welding process	GTA/hot and cold wire additions
Filler metal	16-8-2
Final heat treatment[a]	1060°C (1940°F), ½ h in argon

(a) Heat treatment after radiographic inspection, followed by water quench.

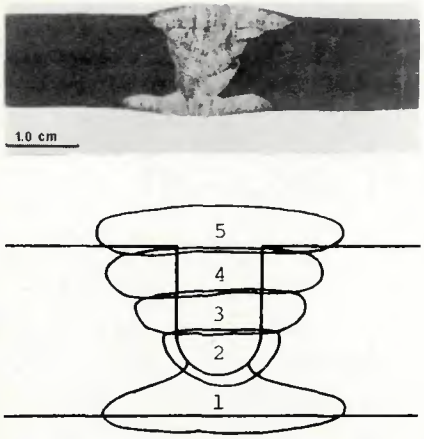

Fig. 1—Macroetched view of weldment section studied with pass sequence: 1—oscillated cold-wire GTAW; 2—cold-wire GTAW (root pass); 3—hot-wire GTAW; 4—oscillated hot-wire GTAW; 5—oscillated hot-wire GTAW

Code specifications. Table 1 summarizes the fabrication data. Subsequent to the postweld solution-anneal, the pipe was subjected to "sizing and straightening" to eliminate the distortion from residual stress recovery during annealing. This introduced some cold-work into the pipe section. The "formed + welded + solution-annealed + straightened" condition is henceforth referred to as an "as-received" one. A transverse weldment section from pipe in this condition was used for this study. The section was then re-solution-annealed at 1065°C (1949°F) for 0.5 hour (h) in argon, air-cooled, and re-examined. Characterization was thus conducted on the weldment in both "as-received" and "reannealed" conditions.

Table 2—Welding Parameters for GTA Seam Weld

No. passes	5
Welding position	Flat
Filler metal	3/32 in. diam, 16-8-2 Cr-Ni-Mo
Inert gas	20% Ar, 80% He @ 50 cfh
Current	DCSP
Amperage, A[a]	Inside pass—400; root pass—250-275; rem. passes—up to 400
Feed speed (FS)	6 ipm on inside pass; 8 ipm on root pass; 9 ipm on rem. passes
Heat input rate,[b] joules/in.	$4.4 - 5.6 \times 10^4$ on inside pass, $2.1 - 2.9 \times 10^4$ on root pass; $< 3.7 \times 10^4$ on rem. passes
Preheat, °F	60 min. on all passes; 300 max. on inside pass.

(a) Voltage, V = 11–14 on all passes.
(b) Heat input rate = A·V/FS.

Table 3—Chemical Analysis of Formed and Welded Pipe (Ref. 5), Wt-%

	Plate	Weld
C	0.066	0.053
Mn	1.63	1.57
P	0.032	0.014
S	0.009	0.014
Si	0.58	0.49
Ni	11.29	9.42
Cr	16.09	16.18
Mo	2.85	1.95
V	0.06	0.04
Nb	< 0.01	< 0.01
Ti	0.01	0.01
Co	0.17	0.06
Cu	0.22	0.13
Al	0.01	< 0.01
B	0.001	0.001
N	0.039	0.041

Figure 1 is a macroetched view of the transverse weldment section studied, with the welding pass sequence. Table 2 details the actual welding parameters employed, and Table 3 is a spectrographic chemical analysis of the plate (base metal away from weld) and weld metal (from center of weld with minimum dilution).

Microscopy

Optical. Optical microscopy on the base metal, heat-affected zone (HAZ) and weld metal regions enabled a characterization of the grain structure and the absence of any effect of reannealing on it. Figure 2 shows the typical weld metal and base metal grain structure. The quantitative information on grain sizes estimated by a random line-intercept technique indicates (Table 4) that the weld and base metal grain sizes are comparable. Also, no significant grain coarsening was visible in the HAZ areas.

Figure 3 is the optically observed typical weld metal dendritic substructure with approximately a 2% by area QTM globular delta ferrite (Ref. 5) in the "as-received" condition. Reannealing only very slightly coarsened the substructure with no measurable change in the size, content, and distribution of ferrite. The secondary interdendritic arm spacing was visually estimated at about 1–3 μm.

The location of ferrite (inter- or intradendritic) was difficult to determine optically. It must be mentioned that TEM observations indicated ferrite globules varied in size from 0.7 to 6.0 μm with a large fraction between 1.5 and 2.5 μm before reannealing. Reannealing appeared to decrease the maximum and median size. In both the "as-received" and "reannealed" welds, ferrite was generally found (~two-thirds of ferrite observed) not associated with any dislocation boundaries, which—from the succeeding discussion on dislocation boundaries—indicates it to be mostly intradendritic.

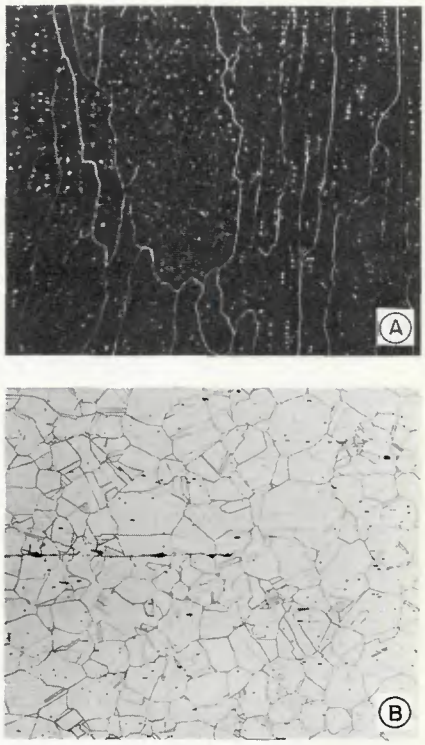

Fig. 2—A comparison of weld metal Ⓐ and base metal grain structures Ⓑ. The dark field in Ⓐ enables better grain boundary definition. Electrolytically etched using 50 HNO_3; 50 H_2O

TEM. Thin foils about 0.3 μm thickness were examined on a JEOL-Model JEM 200A electron microscope operated at 200 kV. The microscope was equipped with a 30 deg tilt-360 deg azimuth (tilt axis position) specimen stage enabling defect characterization. To prepare the foils, 2.5 mm (0.1 in.) square × 0.4 mm (0.016 in.) thin elements were sectioned from the weldment of Fig. 1 so that the element thickness was parallel to the pipe wall thickness dimension. Aproximately 20 elements from each weldment (as-received and reannealed) representing various locations in the base metal, HAZ and weld metal were selected. These were next ground to ~0.15 mm (0.006 in.) thickness and electropolished to per-

Table 4—Average Grain Intercept (μm)

Region	Weld pass	Size, μm
Weld	Outside	128
	Root	87
HAZ	Outside	121
	Center	106
	Inside	113
Base	Outside	132
	Center	73
	Inside	114

foration in a 90:10 acetic acid:perchloric acid by volume electrolyte using a twin-jet technique at 40 volts (V) and a current density of 1.75 amperes (A)/cm^2.

A single grain representing the "average" dislocation structure for that foil, estimated visually, was selected for characterization. Characterization included, where possible, a measure of:

1. Dislocation density, ρ (cm^{-2}), estimated from two-dimensional micrographs taken under a variety of two-beam conditions using Ham's technique (Ref. 6).

2. Dislocation Burgers vector, $\vec{b}$, and line direction, $\vec{t}$; after determining the grain orientation with respect to the incident electron beam under fixed conditions of tilt and azimuth (represented by a stereographic projection), the Burgers vector was determined using the $\vec{g} \cdot \vec{b} = 0$ criterion for invisibility, where $\vec{g}$ is the operating diffracting beam vector (for edge dislocations of the

$$\vec{b} = \frac{a}{2} <110>$$

kind, where a is the lattice parameter, $\vec{g} \cdot \vec{b} \times \vec{t}$ is too small for a visible image with $\vec{g} \cdot \vec{b} = 0$) (Ref. 7).

3. Subgrain or substructure size, λ (μm), obtained from two-dimensional micrographs in a manner as for grain size estimation.

4. Subboundary or low-angle dislocation boundary misorientation, Θ (deg), measured by the shift in a Kikuchi line intersection in traversing the boundary.

Details on TEM methods used may be found in the literature (Ref. 8).

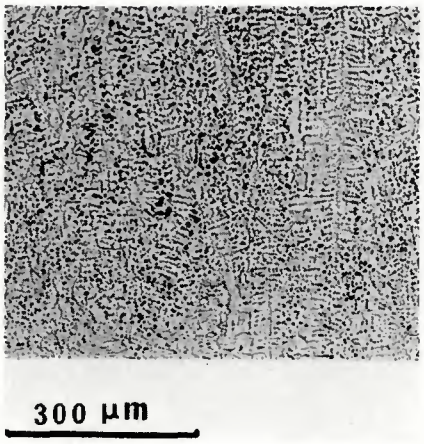

Fig. 3 — Typical weld metal dendritic structure viewed optically with approx. 2% QTM globular delta-ferrite. Electrolytically etched using 50 HNO_3: 50 H_2O

Results and Discussion

General Substructure Characterization

The microstructure as a function of location in the "as-received" weldment section is visible in Fig. 4. The accompanying microhardness numbers are shown as strength estimates obtained at room temperature with a 500 g load and 136 deg diamond pyramid hardness (DPH) indentor. The obvious difference in weld and base metal microstructure is the existence of curved low-angle dislocation boundaries (subboundaries) in the weld, not seen in the base metal. Areas in base metal exhibit a random dislocation distribution with no segregation into subboundaries. Table 5 summarizes some measured aspects of the dislocation structure with the hardness values for locations described in Fig. 4.

Within a given zone of weldment (base metal, HAZ, or weld) microstructural variation is more evident across the pipe wall than along the circumference. Pipe straightening not only accounts for a dislocation density higher than normally observed for solution-annealed material, but also results in the variations in microhardness and dislocation density seen across the pipe wall (non-uniform cold-work across pipe thickness).

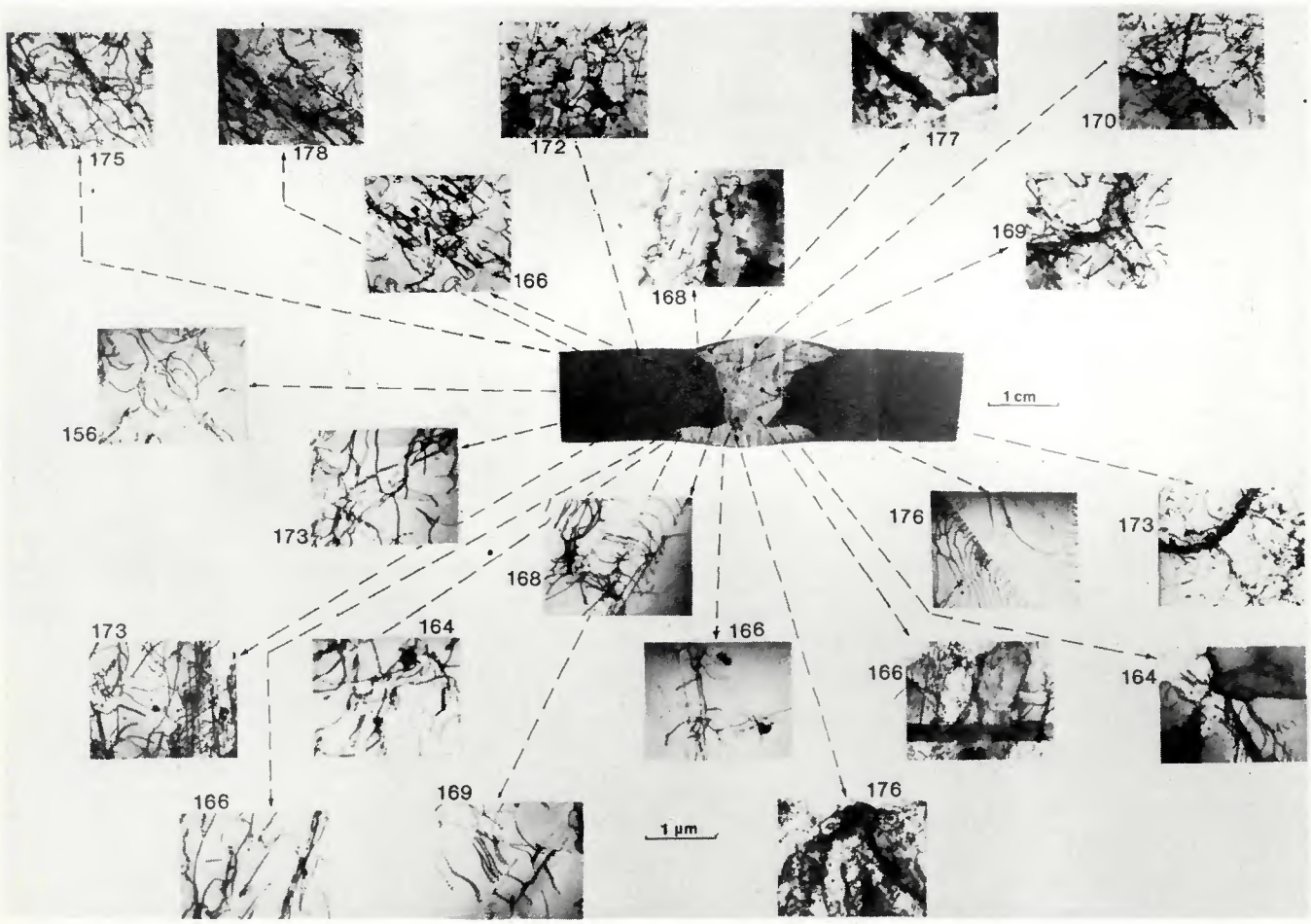

Fig. 4 — TEM structures and microhardnesses for different locations in the "as-received" weldment section

Table 5—Dislocation Structure Evaluation and Microhardness for Specific Locations in GTA Weldment As-received

Zone	Location[a]		Microhardness DPH (kg/mm²)	Average[b] dislocation density ρ, (cm^{-2}) $\times 10^9$	Subboundaries: Average misorientation, deg	Subboundaries: Estimated[c] substructure size, μm
Base Metal	Outside	11	175	6.46	No subboundaries	
		12	178	5.07		
		13	172	7.03		
		31	156	1.83		
	Inside	51	173	5.93		
Heat-Affected Zone	Outside	21	166	5.66	No subboundaries	
		22	168	4.50		
		32	173	3.15		
		41	164	2.69		
		44[d]	164	4.02	0.68	1.2
	Inside	52	166	2.24	No subboundaries	
Weld Metal	Outside	14	177	N.M.[e]	0.34	2.8
		15	170	N.M.	0.38	2.5
		23	169	N.M.	0.46	2.3
		33	168	2.90	0.37	2.3
		34	176	1.55	N.M.	N.M.
		35	173	4.61	N.M.	2.8
		42 root	166	1.97	No subboundaries	
		43 pass	166	3.80	No subboundaries	
		53	169	2.00	N.M.	N.M.
	Inside	54	176	N.M.	0.57	1.7

(a) XY location in Fig. 4: X—row from outside to inside with increasing number; Y—location examined from left to right along row.
(b) Measured from regions of foil with no subboundaries.
(c) Two-dimensional line intercept estimate.
(d) Probably from weld since very close to fusion zone boundary.
(e) N.M.—not measured.

For the base metal and HAZ, dislocation densities and hardness values were generally higher nearer the pipe surfaces and decreased toward the center. The weld metal has a dislocation substructure of size comparable with the optically-estimated interdendritic arm spacing, and appearing to decrease somewhat with a smaller bead cross-section (or lower heat-input rate). The "subgrains," which are regions of crystal separated by subboundaries, had average misorientations between neighbors of the order of 0.5 deg, also appearing to decrease with a decreasing heat input rate. In fact, subboundaries at the root pass with the lowest heat-input rate are believed to have energies or misorientations so low as to be very poorly-defined and characterized as "absent."*

Reannealing resulted in a lowering of hardness and random dislocation density everywhere with the persistence of subboundaries in the weld metal region. Figure 5 and Table 6 are complete microstructural descriptions of the "reannealed" weldment. In the base metal and HAZ the dislocation density and hardness decreased such that regions of higher density and hardness before reannealing became regions of lower density and hardness after the reanneal. Data on microhardness and dislocation density in Tables 5 and 6 were used to evaluate the strengthening effect (measured by room temperature microhardness) of random dislocations, some of which are as a result of pipe straightening. Only data on base metal and HAZ was used. Figure 6 shows the strengthening as a linear function of the square root of dislocation density, $\sqrt{\rho}$, representing the forest hardening effect of random dislocations.

Reannealing of the weld metal resulted in a slight coarsening of the substructure (increase in substructure size) accompanied by an apparent increase in the subboundary misorientation, the decreasing size and misorientation with decreasing bead width or heat-input rate being maintained. The persistence of subboundaries in the weld results in a "residual" weld metal strength even after reannealing manifesting itself as a somewhat higher than base metal weld metal hardness. Subboundaries have been shown to strengthen by reducing the effective grain size in a Hall-Petch fashion. Reannealing effected some recovery of the cold-work in straightening and no recrystallization in either weld or base metal regions.

Thus, the optically visible weld metal dendritic structure appears as a dislocation substructure when viewed through the TEM, the "optical" dendritic arm spacing being comparable with the TEM estimated substructure size. Also, the subboundaries, as will be shown below, have characteristics indicating they occur as a result of solidification and correspond to the interdendritic etched areas seen optically.

Solidification, and consequently substructure characteristics, are complex functions of local undercooling in the melt, dependent on a variety of process and material parameters (Ref. 9). For this reason, a quantitative correlation between the two substructure characteristics measured (size and boundary misorientation) and a single parameter such as weld heat-input rate is not attempted here. In general, however, factors such as a low heat-input rate resulting in a faster cooling rate (G.R, G w thermal gradient in melt, R w growth rate) effect a finer substructure. Factors contributing to a reduction in G/R or an increased propensity for dendritic growth effect higher energy and higher misorientation (tighter, more dislocation dense) subboundaries.

Subboundary Characterization

Fifteen subboundaries or networks from the weld metal regions of both the "as-received" and "reannealed" weldments were analyzed. Since the subboundaries in both cases had identical characteristics, these are discussed without specific reference to the weldment condition.

The manner of subboundary charac-

For a subboundary misorientation, $\theta \leq 0.2$ deg, the density, ρ, of dislocations in a subboundary $\simeq$ that observed in a "solution-annealed" random dislocation structure ($\sim 10^8$ cm^{-2}): $\rho = 1/d^2$, where d = mean dislocation spacing (cm) in boundary estimable from: $d = |b|/\theta$ (rad.).

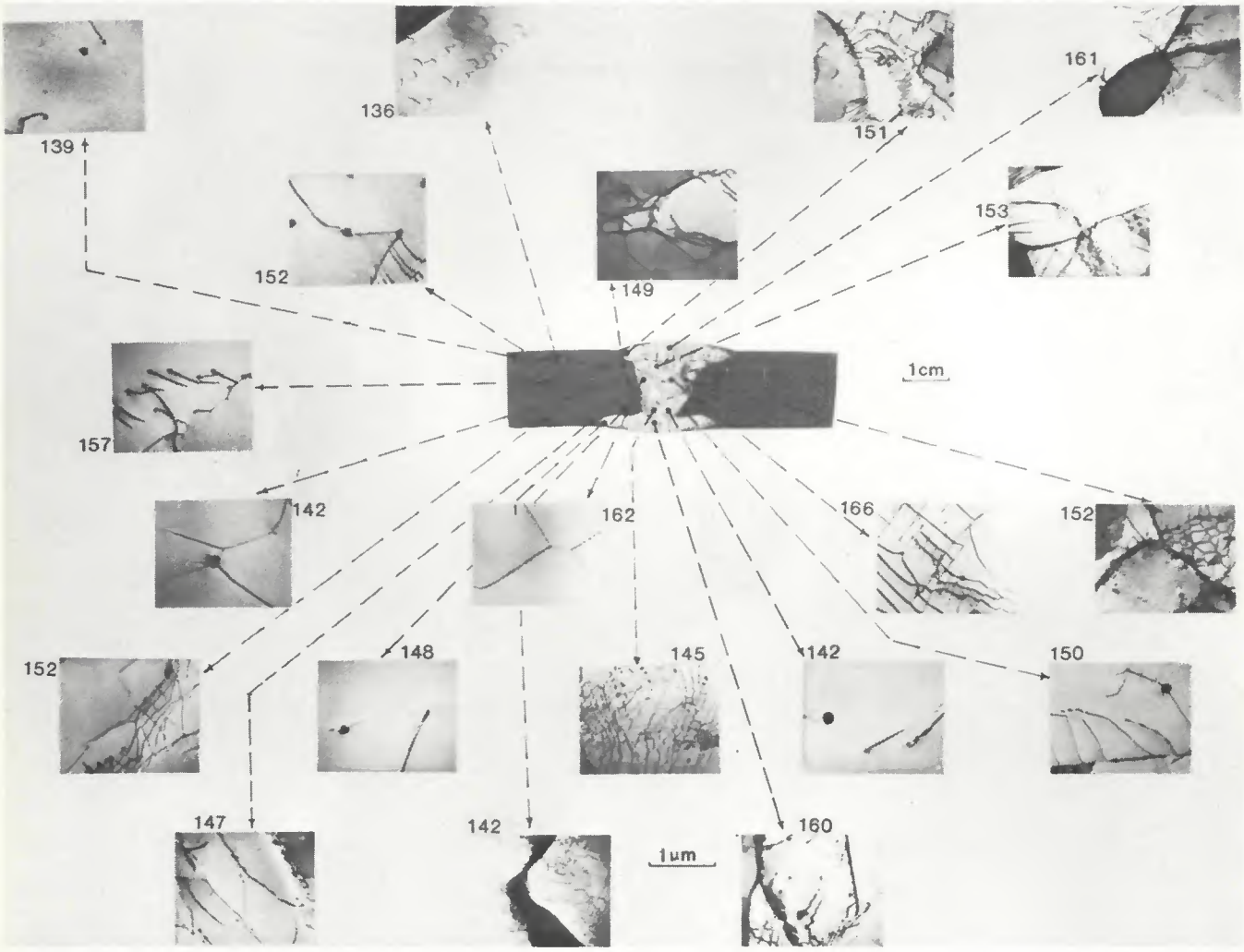

Fig. 5 — TEM structures and microhardnesses for different locations in the "reannealed" weldment section

terization carried out is based on the various mechanisms proposed by Lindroos and Miekk-oja for their formation (Ref. 10). Curiously, they recognized rapid solidification as a means of generating dislocation substructures to study their influence on deformation. Following are a few definitions of terms used to describe the boundaries:

- Forest plane: this is the plane of the network and contains the dislocations making up the boundary. In cases where the network exhibits a curvature the forest plane is continuously varying and determined from analysis over a limited region of boundary.
- Forest dislocations: these are one or more families of line defects lying in the forest plane, often sessile and forming the basis for a network.
- Glide-source dislocations: these are dislocations produced within the crystal (not at the forest) capable of moving under stress, which on reaction with the forest dislocations result in a network.
- Junction dislocations: these are produced as a result of reaction between a glide-source dislocation and a forest dislocation; since observation of the network cannot differentiate between a glide-source and a junction dislocation segment, all segments not of the 'forest' kind are referred to as junction dislocations.
- Node: this refers to the joint common to several dislocation segments in the network, usually 3-fold with three being the number of segments at the point.
- Burgers vector plane: the plane defined by and containing the Burgers vectors of the segments at a node.

The subboundaries examined were all curved hexagonal networks (Fig. 7 Ⓐ), the dislocation segments at each node being nearly coplanar. Of the three dislocation families, the "forest" one was easily distinguishable by the large edge component in its Burgers vector. Junction dislocations are generally expected to have small edge components if the glide-source dislocation is of strong screw character.

Figure 7 Ⓑ details a typical network examined. Note the large edge character of the forest dislocation family "C" and the nearly pure screw nature of the junction dislocation families "A" and "B."

Table 7 shows results on the forest planes of subboundaries analyzed. The large edge character of the "immobile," "non-glide" forest dislocations and the often approximate {110} boundary as forest plane* support the theory that "polygonization" or "build-up" occurs on dislocations (forest) accommodating the mismatch between adjacently solidifying dendrites or dendrite arms.

The last to solidify interdendritic regions are the ones accommodating the crystallographic mismatch (misorientation) between the adjacently grown dendrites in the "growth substructure." This explanation of rapid growth first proposed by Rutter and Chalmers (Ref. 11) is consistent with actual observations on the substructure (Ref. 12), also seen here. The mismatch regions — interdendritic in

**The approximate {110} mismatch plane with its curvature suggests the deviation from classical prismatic growth expected with dendritic solidification; it also supports its existence as an interdendritic mismatch plane.*

Table 6—Dislocation Structure Evaluation and Microhardness for Specific Locations in GTA Weldment Reannealed

Zone		Location[a]	Microhardness DHP (kg/mm²)	Average[b] dislocation density ρ, (cm^{-2}) × 10^9	Subboundaries: Average misorientation, deg	Subboundaries: Estimated[c] substructure size, μm
Base Metal	Outside	11	139	0.33	No Subboundaries	
		12	136	0.46		
		21	152	0.55		
		31	157	0.82		
	Inside	51	152	0.60		
Heat-Affected Zone	Outside	22	149	2.34	No Subboundaries	
		32	142	0.35		
		41	148	0.39		
	Inside	62	147	1.95		
Weld Metal	Outside	13	151	2.14	0.69	2.3
		14	161	0.40	0.68	4.0
		23	153	0.62	0.43	4.2
		33	162	0.34	0.40	2.2
		34	166	0.92	0.37	2.5
		35	152	0.64	N.M.[d]	5.0
		42 root	145	0.58	N.M.	1.4
		43 pass	152	0.36	—No subboundaries—	
		44	150	0.98	—No subboundaries—	
		53	142	0.55	0.75	3.6
	Inside	54	160	0.57	0.62	3.7

(a) XY location in Fig. 5: X—row from outside to inside with increasing number; Y—location examined from left to right along row.
(b) Measured in regions of foil with no subboundaries.
(c) Two-dimensional line intercept estimate.
(d) N.M.—not measured.

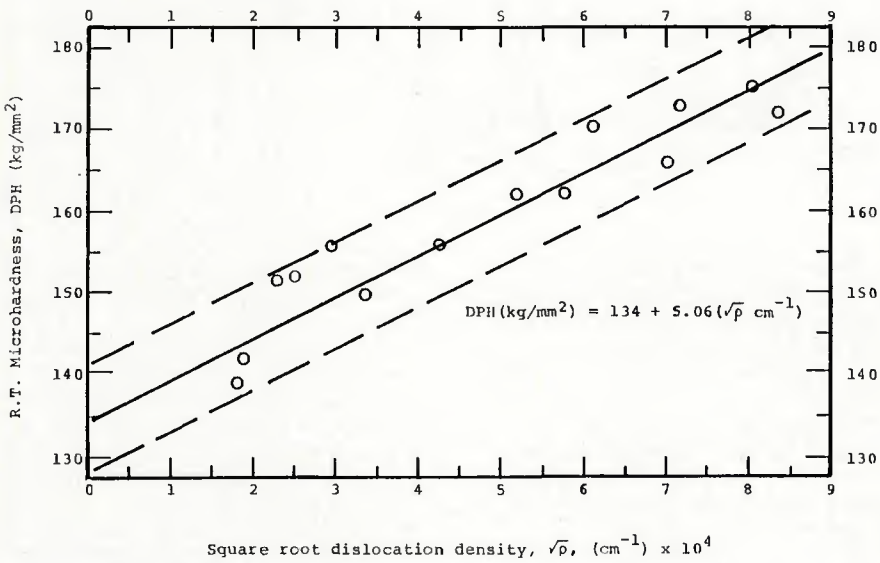

Fig. 6—Strengthening effect of random dislocations in base metal

this case—comprise a system of dislocations at least locally planar and capable of accommodating a relative "twist" about an axis perpendicular to this plane (twist boundary), a "tilt" about an axis in the plane of the boundary (tilt boundary), or both a tilt and twist (tilt "n" twist boundary) about two orthogonal axes (Ref. 13).

The plane here is called a "forest plane" and the accommodating dislocations—"forest dislocations." Evidently these dislocations by the very nature of their creation seldom belong to the slip systems, primary or conjugate, of either dendrite at the forest plane. The networks or subboundaries seen after solidification are often the result of mobile glide-source dislocations from intradendritic regions interacting with the forest dislocations either during cooling or postweld stress/temperature treatments.

The process of substructure formation is similar to the "microscopic polygonization" observed with recovery after "turbulent" flow in FCC crystals (Ref. 14), wherein interaction of glide dislocations with intracrystalline Cottrell barriers is responsible for the substructure. Deformation substructures like those generated at elevated temperatures, however, comprise dislocations at the subboundary belonging to the matrix glide systems and are therefore distinguishable from the "growth" substructure seen here.

The basic "knitting" mechanism for a hexagonal network described by Lindroos and Miekk-oja (Ref. 10) is reproduced here. Figure 8 Ⓐ shows a (110) forest plane with a system of parallel edge forest dislocations, C, with

$$\vec{b} = \overrightarrow{NP} = \frac{a}{2}[110]$$

intersecting the $(\bar{1}11)$ plane of a Thompson tetrahedron. The pure screw glide-source dislocation, A, with

$$\vec{b} = \overrightarrow{MN} = \frac{a}{2}[\bar{1}0\bar{1}]$$

on the $(\bar{1}11)$ plane glides toward the forest under a shear stress, τ. A and C align by climb [that dislocations reacting at elevated temperatures always form attractive junctions through alignment by vacancy transport along dislocation cores has been demonstrated (Ref. 15)] and react as shown in Fig. 8 Ⓑ:

$$\overrightarrow{MN} + \overrightarrow{NP} \rightarrow \overrightarrow{MP} \text{ or } \frac{a}{2}[\bar{1}0\bar{1}] + \frac{a}{2}[110] \rightarrow \frac{a}{2}[01\bar{1}],\ A + C \rightarrow B$$

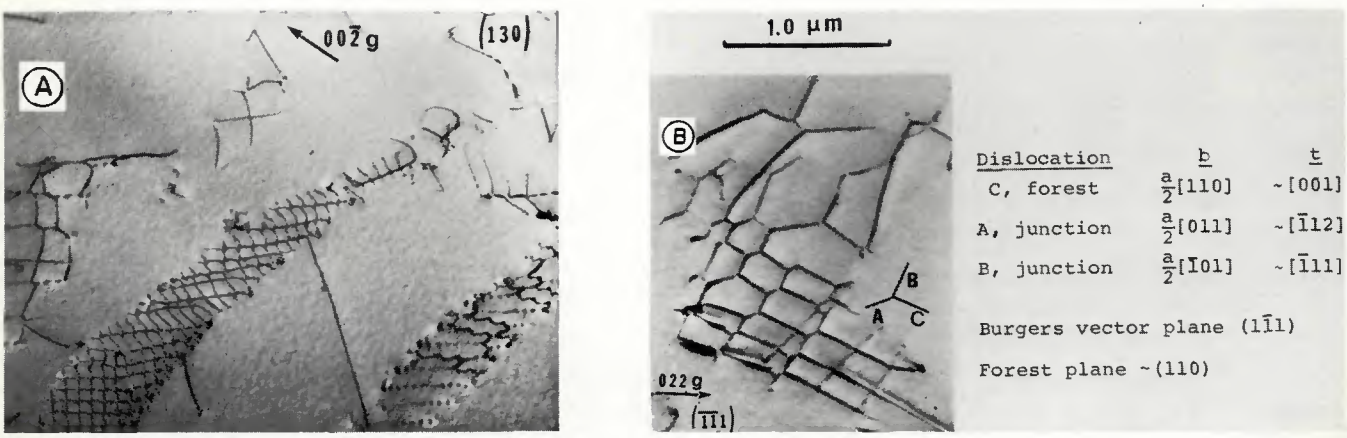

Fig. 7 — Subboundary networks: Ⓐ— typical curved low-angle dislocation boundary in weld metal; Ⓑ— analysis of a hexagonal network comprising a subboundary

Table 7—Number of Subboundaries with a Given Forest Plane

Forest plane	No. of subboundaries
(111)	2
(110)	11
(112)	2

The junction dislocation, B, has a Burgers vector,

$$\overrightarrow{MP} = \frac{a}{2}[01\bar{1}]$$

lying in the forest plane and not being in its normal glide plane, being held there by elastic and/or chemical forces. Its line tension pulls dislocation A onto the same plane. In identical fashion, junction dislocations are formed at all forest dislocations and the hexagonal network of Fig. 8 Ⓑ established.

Various other more complex mechanisms based on the same principle of attractive junction formation by stress-induced climb have been proposed, resulting in a variety of networks (Refs. 10, 16, 17, 18). It is noted that the curvature in the network is effected by increasing or decreasing line segments with corresponding increases and decreases in their Burgers vector edge components respectively. Also, the very nature of the knitting mechanism and subboundary suggests a possible recovery mechanism (Ref. 17) important to elevated temperature weld metal deformation.

The stability of the subboundaries, evidenced by their persistence on reannealing, attests to their low energy. From an approximate theoretical estimate of the boundary energy using (Ref. 19):

$$\epsilon = E_o\Theta(A - \ln\Theta), \text{ where } E_o = \frac{Gb}{4\pi(1-\nu)}$$

where $A = \ln(b/b_o)$ and Θ = misorientation (radians); b = Burgers vector of dislocation; b_o = dislocation core radius (~b); G = elastic shear modulus; ν = Poisson's ratio; ϵ = energy/unit boundary area.

The energy for a low-angle (<1.0 deg) boundary is less than one-fifth that of a normal grain boundary which does not exceed $\epsilon_m = E_o\Theta_m$ where $\Theta_m = \exp(A - 1)$. For ϵ_L = low-angle boundary energy,

$$\epsilon_L/\epsilon_m \approx \frac{E_o(1.75 \times 10^{-2})(A + 4.05)}{E_o[\exp(A-1)]}$$

$$\approx 0.2 = \frac{1}{5} \text{ for } A \approx 0.$$

It seems obvious that their low energy (representing a barrier to recrystallization) and inherent immobility make these subboundaries a fairly stable aspect of the weld metal microstructure.

Polygonization, the formation of meshes or networks usually with post-weld stress-relief treatments, has been briefly previously reported (Refs. 20, 21). However, it was not given due attention with regard to its role in weld metal deformation behavior. Even in the absence of a postweld heat treatment, subboundaries are expected to occur as one or more families of "forest" or "mismatch" dislocations, not necessarily as a well-defined network or mesh and therefore not easily distinguishable from random glide dislocations, except by analysis. Forest boundaries of this type are further masked by the higher total dislocation density of the "as-welded" condition prior to any postweld stress-relief (Ref. 20).

The inevitable polygonization of weld metal dislocations with post-weld heat treatments confirms the existence of forest dislocations in subboundaries. Subboundaries in whatever form, however,

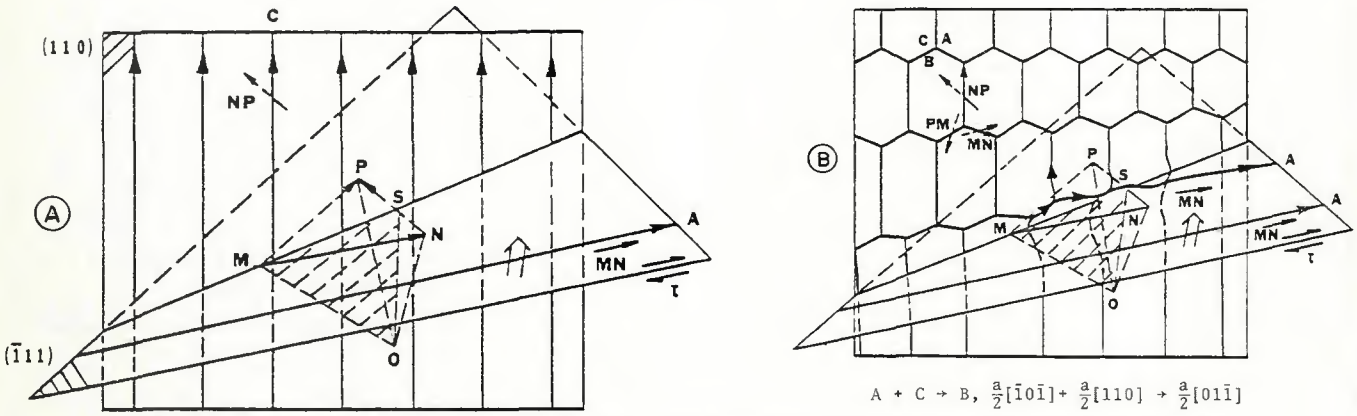

Fig. 8 — A knitting mechanism after Lindroos and Miekk-oja (Ref. 10) for the formation of a subboundary with a hexagonal network

are expected to influence weld metal behavior in the same fashion.

Conclusions

Following are the conclusions derived from this characterization study:

1. The base metal had a random dislocation structure (no subboundaries) shown to effect strengthening in a forest hardening fashion. The weld metal, however, exhibited a *stable* dislocation substructure comprising low-angle (<1.0 deg.) subboundaries and having a size comparable with the interdendritic arm spacing.
2. The residual weld metal strength after reannealing, manifesting itself as a weld metal hardness greater than the base metal hardness, may be attributed to the strengthening effect of these stable, persistent subboundaries in the weld, realizing a decrease in effective grain size.
3. Within the weld metal zone the substructure size and subboundary misorientation appeared to decrease with bead width or heat-input rate.
4. Subboundary analysis indicated a "build-up" or "polygonization" on "forest" or "growth" dislocations accommodating the mismatch between adjacently solidifying dendrites.
5. The proposed mechanism for this "polygonization" or "knitting" appears valid based on the analysis conducted.

Results point to the existence of subboundaries as inevitable in weld pool solidification.

It has been the object of this paper to characterize in detail the weld metal dislocation substructure, and by demonstrating its existence as a consequence of rapid solidification, extend these results to all conventional weld systems. This represents the first stage in a different, but universally applicable approach to the understanding of weld metal deformation behavior based on its apparently stable solidification substructure.

Acknowledgments

The authors acknowledge Dr. V. K. Sikka and Dr. J. W. McEnerney of the Oak Ridge National Laboratory for making available the specimens for this study.

References

1. Klueh, R. L., and Edmonds, D. P. 1980 (September). *Mechanical properties of 16-8-2 large-diameter pipe girth welds.* Oak Ridge National Laboratory Report ORNL-S660.
2. ASME Boiler and Pressure Vessel Code, Section II, Material Specification Part A, Ferrous Materials, SA-240. *Specification for chromium and chromium-nickel stainless steel plate, sheet and strip for fusion-welded unified pressure vessels.* ASME, 1974 ed., through summer 1975 addenda.
3. ASME Boiler and Pressure Vessel Code, Section II, Material Specification Part A, Ferrous Materials, SA-358. *Specification for electric-fusion-welded austenitic chromium-nickel alloy steel pipe for high temperature service.* ASME 1974 ed., through summer 1975 addenda.
4. ASME Boiler and Pressure Vessel Code, Section III, Division 1, Nuclear Power Plant Components, Subsection NB-Class 1 Components. ASME 1977 edition, through summer 1975 addenda.
5. McEnerney, J. W., and Sikka, V. K. 1979 (April). *Characterization of Time-Independent Properties of Formed and Welded Pipe for Breeder Reactor Applications.* Oak Ridge National Laboratory Report, ORNL/TM-6609.
6. Ham, R. K. 1961. The determination of dislocation densities in thin films. *Phil. Mag.* 6: 1183-84.
7. Hirsch, P. B.; Howie, A.; Nicholson, R. B.; Pashley, D. W.; and Whelan, M. J. 1965. *Electron microscopy of thin crystals,* 181-82. London: Butterworths.
8. Foulds, J. R. 1981. *Substructure of 316 stainless steel pipe weldments;* 217-25. Ph.D. dissertation, University of Cincinnati.
9. Davies, G. J., and Garland, J. G. 1975. Solidification structure and properties of fusion welds. *International Metallurgical Reviews,* Rev. #196, 20: 83-106.
10. Lindroos, V. K., and Miekk-oja, H. M. 1967. The structure and formation of dislocation networks in aluminum-magnesium alloys. *Phil. Mag.* 16: 593-610.
11. Rutter, J. W., and Chalmers, B. 1953. A prismatic substructure formed during solidification of metals. *Canad. J. Physics* 31: 15-39.
12. Hulme, K. F. 1954. Note on the disorientation and impurity substructures in zinc single crystals. *Acta Met.* 2: 810-815.
13. Weertman, J., and Weertman, J. R. 1964. *Elementary dislocation theory:* 187-96. New York: McMillan.
14. Friedel, J.; Boulanger, C.; and Crussard, C. 1955. Elastic modulus and internal friction of polygonized aluminum [and aluminum alloys]. *Acta Met.* 3:380-91.
15. Turunen, M. J., and Lindroos, V. K. 1974. Model for dislocation climb by a pipe diffusion mechanism. *Phil. Mag.* 29: 701-08.
16. Miekk-oja, H. M. 1966. A mechanism for knitting the dislocation network. *Phil. Mag.* 13: 367-70.
17. Lindroos, V. K., and Miekk-oja, H. M. 1968. Knitting of dislocation networks by means of stress-induced climb in an aluminum-magnesium alloy. *Phil. Mag.* 17: 119-33.
18. Miekk-oja, H. M. and Lindroos, V. K. 1972. The formation of dislocation networks. *Surface Science* 31: 422-55.
19. Friedel, J. 1974. *Dislocations:* 284-288. Massachusetts: Addison-Wesley.
20. DeRosa, S.; Jacobs, M. H.; Jones, D. G.; and Sherhod, C. 1979. Studies of TIG weld pool solidification and weld bead microstructure in stainless steel tubes. *Solidification and casting of metals:* 416-23. U.K.: The Metals Society.
21. King, R. T.; Canonico, D. A.; and Brinkman, C. R., 1975. Elevated temperature weldment behavior as related to nuclear design criteria. *Welding Journal* 54(4): 130-s to 140-s.

WRC Bulletin 269
August 1981

Interpretive Report on Dynamic Analysis of Pressure Components—Second Edition

This report is the first update of WRC Bulletin 246, February 1979. It summarizes the state-of-the-art in the four most important areas of dynamic analysis: 1) Dynamic Modeling; 2) Pipe Rupture Phenomena and Missile Impact; 3) Fluid Pressure Transients; and 4) Seismic Analysis and Related Effects.

This Second Edition was prepared by the Subcommittee on Dynamic Analysis of Pressure Components of the Pressure Vessel Research Committee. It will be used as a guide for all future research of the Subcommittee to help avoid duplication of effort.

The price of WRC Bulletin 269 is $10.75 per copy plus $3.00 for postage and handling. Orders should be sent with payment to the Welding Research Council, 345 E. 47th St., New York, NY 10017.